

Article

Short-Circuit Current Calculation and Harmonic Characteristic Analysis for a Doubly-Fed Induction Generator Wind Turbine under Converter Control

Jing Li *, Tao Zheng and Zengping Wang

State Key Laboratory for Alternate Electrical Power System with Renewable Energy Source, North China Electric Power University, Beijing 102206, China; zhengtao_sf@126.com (T.Z.); wangzp1103@sina.com (Z.W.)

* Correspondence: lijing_ncepu@ncepu.edu.cn; Tel.: +86-158-1146-2585

Received: 30 August 2018; Accepted: 14 September 2018; Published: 17 September 2018



Abstract: An accurate calculation of short-circuit current (SCC) is very important for relay protection setting and optimization design of electrical equipment. The short-circuit current for a doubly-fed induction generator wind turbine (DFIG-WT) under excitation regulation of a converter contains the stator current and grid-side converter (GSC) current. The transient characteristics of GSC current are controlled by double closed-loops of the converter and influenced by fluctuations of direct current (DC) bus voltage, which is characterized as high order, multiple variables, and strong coupling, resulting in great difficulty with analysis. Existing studies are mainly focused on the stator current, neglecting or only considering the steady-state short-circuit current of GSC, resulting in errors in the short-circuit calculation of DFIG-WT. This paper constructs a DFIG-WT total current analytical model involving GSC current. Based on Fourier decomposition of switch functions and the frequency domain analytical method, the fluctuation of DC bus voltage is considered and described in detail. With the proposed DFIG-WT short-circuit current analytical model, the generation mechanism and evolution law of harmonic components are revealed quantitatively, especially the second harmonic component, which has a great influence on transformer protection. The accuracies of the theoretical analysis and mathematical model are verified by comparing calculation results with simulation results and low-voltage ride-through (LVRT) field test data of a real DFIG.

Keywords: doubly-fed generator; converter control; short-circuit current; second harmonic component; low-voltage ride-through (LVRT) field test data

1. Introduction

With the worsening global energy crisis and environmental pollution, renewable energy sources have received worldwide attention and undergone rapid development. The doubly-fed induction generator wind turbine (DFIG-WT) is one of the most popular wind turbine generators due to its low manufacturing cost, high efficiency, and high flexibility, and is extensively applied on wind farms [1–3]. In earlier studies, DFIG-WT was regarded as a load or synchronous generator for short-circuit calculation, as the capacity of wind farms is small [4,5]. However, with the increasing capacity of wind power access to the grid, the influence of the short-circuit current (SCC) of DFIG-WT can no longer be ignored. Since accurate SCC calculation is very important to protection settings [6,7], equipment selection, and the optimal design of wind turbine control strategies [8,9], transient characteristics analysis and the SCC calculation model for DFIG-WT have attracted the attention of researchers around the world in recent years.

Grid codes require that wind turbines must remain connected during specific fault conditions and support the grid voltage by providing a reactive current with a magnitude proportional to the voltage

deviation. A quick response of reactive current provision is also required, and the response times are explicitly stipulated in the grid codes; for example, it is less than 75 ms in the Chinese criteria [10], and is even more strict in the German criteria, with a value of 20 ms [11]. To comply with the grid code requirements, a crowbar circuit is often utilized by the rotor for protection against excessive current. The short-circuit current characteristics of DFIG-WT with crowbar protection have been extensively discussed [12–14]. However, the crowbar operation is not desired due to the loss of controllability and absorption of reactive power.

Under non-severe fault conditions or for some DFIG-WTs with a higher tolerance for voltage drops, excitation control of converters is retained during a fault. Due to different constrictions compared with traditional generators and inverter interfaced generators, the transient characteristic of DFIG-WT under converter control is determined by both electromagnetic equations of the generator and control strategies of the AC-DC-AC converters, and the short-circuit current of DFIG-WT contains the stator short-circuit current and grid-side converter (GSC) short-circuit current.

In evaluating the transient fault characteristics of DFIG-WT, establishing a mathematical analytical model is effective and helpful in obtaining the physical mechanisms and numerical values of electrical quantities. A simplified stator fault current model was built in [15] by neglecting the dynamic process of stator flux linkage and hypothesizing step mutations of the rotor voltage after a fault, but the model could not fit the actual transient short-circuit current completely. A stator current analytical model was presented in [16] by solving a second-order differential equation related to the rotor current of the time domain. This method produced ideal linearization of input and output characteristics of the converter, and did not consider transient responses in the converter. In [17], a more detailed stator current analytical model was constructed based on transfer functions of the control system. However, the sampling delay of the converter and transfer characteristics of pulse-width modulation (PWM) were not considered in this study, resulting in sudden changes of initial short-circuit current at the time of fault occurrence and inaccuracy of transient current calculation. It is mentioned in [18] that the current reference values of the converter should be limited to prevent overcurrent, and the control limits for the rotor side converter were studied in [19]. However, the influence of current limitation of the converter on SSC calculation was not discussed in the above studies. In addition, the analytical SCC models in these studies did not include GSC current.

The influencing factors of GSC short-circuit current were simulated and analyzed in [20], but no analytical model of GSC-transient SCC was constructed. Based on different control targets, a DFIG-WT steady-state short-circuit current model with a consideration of GSC current was constructed in [21]. By comparing the results calculated with and without GSC steady-state current, that study concluded that GSC current should be considered for accurate fault analysis and protection settings, but it only focused on steady-state current and did not mention the transient characteristics of SCC. Since transient characteristics of GSC fault current are influenced by coupling factors, including control strategies of the two-side convertors, transient fluctuation of DC bus voltage, and the electromagnetic transient response of the generator, the construction of a GSC transient current model is more complex than the stator fault current. Existing studies on transient SCC of DFIG-WT have not fully discussed transient characteristics of GSC current. Moreover, there is a lack of theoretical references on calculation errors of transient short-circuit total current caused by neglecting GSC current.

Moreover, most of the models built in the above studies were validated by simulation. As was mentioned in [22], the wind power industry urgently needs validation in comparison with real measurements to verify the accuracy and corresponding usability of the models. Additionally, the validation of a generic DFIG-WT was presented based on a measurement campaign carried out in a real wind farm, which is of great interest to researchers in the field of wind energy. Field test data of a real DFIG-WT are also presented to verify the short circuit current calculation model in this article.

This paper discusses the following to construct a more accurate transient short-circuit current calculation model for DFIG-WT. First, transient response characteristics of GSC and rotor side convertor

(RSC) control systems after a symmetric voltage dip are analyzed based on the transfer functions of the control system. The relation equations among GSC current, DC bus voltage, RSC current, and stator flux linkage are constructed. The coupling mechanisms of the key internal electrical quantities in the converters are thus revealed. Second, the analytical expressions of RSC current, DC bus voltage, and GSC current are deduced based on the above equations. Specifically, a more accurate calculation model of RSC short-circuit current with no sudden changes in the initial time of failure is constructed, considering sampling delay of the control system and small inertial PWM. A detailed calculation model of GSC transient current is established with a consideration of DC bus voltage fluctuation. It was found that there is a high proportion of second harmonic current in the GSC transient fault current, which may result in a false operation of the secondary harmonic restraint relay for transformer protection. Third, the nonlinear characteristics of steady-state fault current of DFIG-WT considering limitations of rotor current are analyzed, and an estimation formula for the maximum steady-state SCC is put forward and verified by simulation. Finally, the accuracy of the theoretical analysis and mathematical models is verified by simulation tests and low-voltage ride-through (LVRT) field test data of a real DFIG. Proportions of GSC current and the second harmonic component in short-circuit total current of DFIG-WT under different fault situations are analyzed.

2. Transient Mathematical Models of DFIG

The electrical parts of DFIG mainly include the induction generator, rotor-side converter, and grid-side converter. RSC and GSC are connected through the DC capacitor [17]. The mathematical models and control strategies of these three parts are briefly introduced in the following section.

2.1. Induction Generator Model

Motor convention is applied on the stator and rotor sides of the induction generator. The magnetic saturation effect is neglected. The mathematical model of the generator in the synchronous reference frame is:

$$\begin{cases} u_s = R_s i_s + j\psi_s + p\psi_s/\omega_1 \\ u_r = R_r i_r + js\psi_r + p\psi_r/\omega_1 \\ \psi_s = L_s i_s + L_m i_r \\ \psi_r = L_r i_r + L_m i_s \end{cases} \quad (1)$$

2.2. RSC Control with Consideration of the Limiting Reference Current

Double closed-loop vector control based on stator voltage orientation was applied on RSC, with the inner loop as the current loop and the outer loop as the power loop. The control mechanism diagram is shown in Appendix A. The reference value of the inner current controller under normal operation control is:

$$\begin{cases} i_{rd0}^* = \min(2L_s P_{s0}^*/3L_m U_{s0}, I_{rd\text{-max}}) \\ i_{rq0}^* = \max(-\frac{U_{s0}}{L_m} - \frac{2L_s Q_{s0}^*}{3L_m U_{s0}}, -\sqrt{I_{r\text{-max}}^2 - i_{rd,opt}^{*2}}) \end{cases} \quad (2)$$

where $I_{rd\text{-max}}$ is the active current-limiting value and $I_{r\text{-max}}$ is the rotor current-limiting value.

When a three-phase short-circuit fault occurs at the terminal of a wind turbine, the outer power loop of RSC will be open and the reference current of the inner current loop will be given directly in order to quickly respond to the terminal voltage dip and fulfill the grid codes, which require wind turbines to have LVRT capability and provide reactive power to support grid voltage recovery. Considering the current limits of RSC, the reference value of the inner current loop during low-voltage circumstances is:

$$\begin{cases} i_{rd1}^* = \min(2L_s P_{s0}^*/(3L_m U_{s1}), \sqrt{I_{r\text{-max}}^2 - i_{rq,lvrt}^{*2}}, I_{rd\text{-max}}) \\ i_{rq1}^* = \max(-U_{s1}/L_m - K_d(0.9 - U_{s1})L_s/L_m, -I_{r\text{-max}}) \end{cases} \quad (3)$$

According to Equation (5) and Figure 1, the current loop of GSC is equivalent to the first-order inertial element and the transfer function is:

$$W_{ci-g}(s) = \frac{i_{gd}(s)}{i_{gd}^*(s)} \approx \frac{1}{1 + s/\omega_{ig}} \quad (6)$$

where ω_{ig} is the bandwidth angular velocity of the inner current loop: $\omega_{ig} = 1/(3T_{sg})$.

The outer voltage loop of GSC focuses on disturbance resistance. The PI parameter of the outer voltage loop of GSC is designed according to a typical second-order system:

$$K_{vP} = \frac{2(\omega_{cv} + 1)C}{3m\omega_1\omega_{cv}T_{ev}}, K_{vI} = \frac{K_{vP}}{\omega_{cv}T_{ev}} = \frac{2(\omega_{cv} + 1)C}{3m\omega_1\omega_{cv}^2T_{ev}^2} \quad (7)$$

where ω_{cv} is the middle frequency bandwidth of the outer voltage loop and T_{ev} is the equivalent time constant of outer voltage loop: $T_{ev} = \tau_v + 3T_s$.

GSC current is determined by its reference value, which is related to DC bus voltage in the outer voltage loop. According to Figure 1 and Equation (6), the d-axis component of GSC current is:

$$i_{gd}(s) = (K_{vP} + \frac{K_{vI}}{s}) \frac{\Delta U_{dc}}{T_{ev}s + 1} + i_{gd0} \quad (8)$$

where ΔU_{dc} is the difference between DC bus voltage and its reference value and i_{gd0} is the initial value of the d-axis component of the GSC pre-fault current. GSC active power is about slip times of stator active power, that is, $P_{g0} \approx -sP_{s0}$. Therefore, $i_{gd0} \approx -sP_{s0}/U_{s0}$.

According to Equation (8), in order to calculate GSC current, it is necessary to obtain the DC bus voltage expression first. It can be seen from Figure 1b that the DC bus post-fault voltage is related to U_{dc}^* , i_{L0} , and Δi_L . DC bus voltage is maintained as constant under the collaborative effect of U_{dc}^* and i_{L0} under normal operating conditions. Under fault conditions, the fluctuation of DC bus voltage ΔU_{dc} is mainly influenced by Δi_L . According to Figure 1b, the transfer function from Δi_L to DC bus voltage U_{dc} is:

$$W_{cv}(s) = \frac{U_{dc}(s)}{\Delta i_L(s)} \approx -\frac{1}{C} \frac{s}{(s - \lambda_1)(s - \lambda_2)} \quad (9)$$

where $\lambda_{1,2}$ is the characteristic roots of Equation (9):

$$\lambda_{1,2} = v \pm \gamma = -\frac{1 + \omega_{cv}}{4\omega_{cv}T_{ev}} \pm \frac{1}{4\omega_{cv}T_{ev}} \sqrt{(\omega_{cv} + 1)(\omega_{cv} - 7)} \quad (10)$$

It is worth noting that Δi_L is the DC-side current of RSC. The transfer relationship between DC-side current and AC-side current of RSC is:

$$i_L = S_a i_{ra} + S_b i_{rb} + S_c i_{rc} \quad (11)$$

Since the switching frequency is significantly higher than the grid fundamental frequency and transient analysis mainly focuses on fundamental frequency, the higher harmonic components can be neglected and only low-frequency components of the switch function are considered. Fourier decomposition of the switch function S_{abc} of RSC is carried out as:

$$\begin{cases} S_a \approx 0.5m \cos(\omega_r t - \delta_r) + 0.5 \\ S_b \approx 0.5m \cos(\omega_r t - \delta_r - 120^\circ) + 0.5 \\ S_c \approx 0.5m \cos(\omega_r t - \delta_r + 120^\circ) + 0.5 \end{cases} \quad (12)$$

where δ_r is the fundamental wave initial phase angle of the switch function.

Based on Equations (11) and (12) and the transfer of RSC current from the stationary reference frame to the synchronous reference frame, the DC-side current of RSC can be expressed as:

$$i_L = \begin{bmatrix} S_a & S_b & S_c \end{bmatrix} C_{2s/3s} \begin{bmatrix} i_{rd} \\ i_{rq} \end{bmatrix} = 0.75m(i_{rd} \cos \delta_r - i_{rq} \sin \delta_r) \quad (13)$$

Equation (13) reflects that the DC-side current of RSC can be calculated according to the AC-side current. In fact, the AC-side current of RSC is equal to the rotor current and is related to the transient response of the inner current loop of RSC.

After the occurrence of the three-phase short-circuit fault on the terminal of the wind turbine, GSC is mainly responsible for maintaining the stability of DC bus voltage. Meanwhile, GSC is also able to generate a small amount of reactive power independently to support the grid voltage [25]. To realize the goal of fast regulation, the outer loop of reactive power is open and the reference value of the inner current loop is given directly after the fault. Referring to Equation (6) and considering fast adjustment of the inner current loop, the q-axis component of GSC current can be regarded as equal to the reference value.

3.2. RSC Transient Response Characteristics

According to the above analysis, in order to calculate the DC bus voltage and GSC current, it is necessary to obtain the RSC current, which is determined by the inner current loop of RSC. The dq-axis structure is symmetric. The control framework of the d-axis is shown in Figure 2.

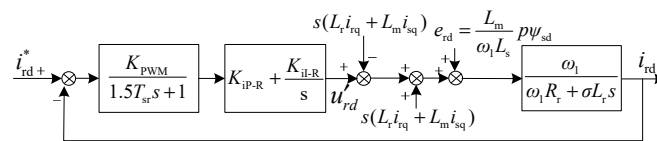


Figure 2. Control framework of inner current loop of RSC.

In Figure 2, K_{ip-R} and K_{il-R} are the proportional gain and integral gain of the PI controller of the inner current controller, respectively; T_{sr} is the switch period of PWM; and e_{rd} is the d-axis component of voltage disturbance.

It can be seen from Figure 2 that changes of reference current i_r^* and voltage disturbance e_{rd} will cause transient responses of RSC. When calculating the transient current of RSC, reference [17] neglected the sampling delay of the converter and small inertial characteristics of PWM, causing the calculated rotor short-circuit current to change suddenly at the moment the fault occurred. In the following section, one more accurate expression of rotor transient current is deduced based on the detailed model of RSC, since rotor current is vital to stator current and GSC current.

Similar to the current loop of GSC, the current loop of RSC can be regarded as a first-order inertial element. The closed-loop transfer function of RSC is:

$$W_{ci-r}(s) = \frac{i_r}{i_r^*} \approx \frac{1}{1 + s/\omega_{ci}} \quad (14)$$

where ω_{ci} is the bandwidth angular frequency of the inner current loop: $\omega_{ci} = 1/(3T_{sr})$.

As stated in Section 3.2, when the terminal voltage drops to lower than 90% U_n , the DFIG-WT will switch to LVRT control and the rotor current reference value will change from a normal operation state (Equation (2)) to an LVRT state (Equation (3)). The rotor transient current caused by sudden changes of the reference value is:

$$\Delta i_{r-ref}(t) = \Delta i_r^* - \Delta i_r^* e^{-\omega_{ci}t} \quad (15)$$

where $\Delta i_r^* = i_{r1}^* - i_{r0}$, i_{r1}^* is the post-fault reference rotor current and i_{r0} is the pre-fault rotor current.

On the other hand, considering the sampling delay of the converter and small inertia of PWM, the closed-loop transfer function from voltage disturbance to transient current of rotor is:

$$W_{ce}(s) = \mathbf{i}_r(s)/\mathbf{e}_r(s) = -\frac{2\omega_{ci}^2}{K_{iP}K_{PWM}} \frac{s[s/(2\omega_{ci}) + 1]}{(s + 1/\tau_i)[(s + \omega_{ci})^2 + (\omega_{ci})^2]} \quad (16)$$

According to the conservation principle of flux linkages, the stator flux linkage after the occurrence of the three-phase short-circuit fault is [26]:

$$\boldsymbol{\psi}_s = \boldsymbol{\psi}_{sf} + \boldsymbol{\psi}_{sn} = -j\mathbf{u}_{s1} - j(\mathbf{u}_{s0} - \mathbf{u}_{s1})e^{-t/\tau_s}e^{-j\omega_1 t} \quad (17)$$

where τ_s is the stator attenuation time constant: $\tau_s = (\sigma L_s)/\omega_1 R_s$.

According to Equation (17), the frequency domain expression of voltage disturbance is:

$$\mathbf{e}_r(s) = j(\mathbf{u}_{s0} - \mathbf{u}_{s1}) \frac{L_m}{L_s} \frac{1/\tau_s + j\omega_1}{s + 1/\tau_s + j\omega_1} \quad (18)$$

Substituting Equation (18) into Equation (16), the transient current of the rotor caused by voltage disturbance is:

$$\Delta \mathbf{i}_{r-er}(t) = \Delta \mathbf{i}_{r1} e^{-j\omega_1 t} e^{-t/\tau_s} + \Delta \mathbf{i}_{r2} e^{-t/\tau_i} + [\Delta \mathbf{i}_{r3} \cos(\omega_{ci} t) + \Delta \mathbf{i}_{r4} \sin(\omega_{ci} t)] e^{-\omega_{ci} t} \quad (19)$$

where $\Delta \mathbf{i}_{r1,2,3,4}$ represents coefficients of attenuation components of the rotor current. The detailed coefficient expressions are shown in Appendix B. These coefficients are related to voltage drop amplitude and parameters of the generator and converter, and meet with $\Delta \mathbf{i}_{r1} + \Delta \mathbf{i}_{r2} + \Delta \mathbf{i}_{r3} = 0$, thus assuring $\Delta \mathbf{i}_{r-er}(0) = 0$ at the initial fault stage.

According to Equations (17) and (19), the time domain expression of the rotor current is:

$$\mathbf{i}_r = \mathbf{i}_{r0} + \Delta \mathbf{i}_r = \mathbf{i}_{r0}^* + \Delta \mathbf{i}_r^* - \Delta \mathbf{i}_r^* e^{-\omega_{ci} t} + \Delta \mathbf{i}_{r-er} \quad (20)$$

In this section, the equations between different electrical quantities, such as GSC current, DC bus voltage, and AC-side and DC-side currents of RSC, are deduced based on control mechanisms of GSC and RSC. Moreover, the coupling relationships and variation laws of the DC capacitor and key electrical quantities of GSC and RSC are revealed.

4. Transient Short-Circuit Current Calculation Model of DFIG-WT

4.1. DC Bus Voltage

DC bus voltage has to be calculated first to obtain the GSC current. According to the transfer function in the DC voltage loop and DC-side current of RSC, the expression of DC bus voltage fluctuation ΔU_{dc} can be deduced according to Equations (9), (13), and (19):

$$\Delta U_{dc}(t) = U_{dc1} \cos(\omega_1 t - \beta_1) e^{-t/\tau_s} + U_{dc2} e^{-t/\tau_i} + U_{dc6} e^{\lambda_1 t} + U_{dc7} e^{\lambda_2 t} + [U_{dc3} \cos(\omega_{ci} t + \beta_2) + U_{dc4} \sin(\omega_{ci} t + \beta_2) + U_{dc5}] e^{-\omega_{ci} t} \quad (21)$$

where U_{dc1} , U_{dc2} , U_{dc3} , U_{dc4} , U_{dc5} , U_{dc6} , and U_{dc7} are coefficients of different components. Detailed expressions are shown in Appendix B.

It can be seen from Equation (4) that the fluctuating DC bus voltage is caused by an active power imbalance between the converters at the two sides. The fundamental frequency attenuation component in RSC current may cause a fundamental frequency attenuation component in U_{dc} . This implies that U_{dc1} corresponds to the fundamental frequency attenuation component $\Delta \mathbf{i}_{r1}$ in the rotor current. Similarly, U_{dc2} , U_{dc5} , U_{dc6} , and U_{dc7} correspond to $\Delta \mathbf{i}_{r2}$, $\Delta \mathbf{i}_{r3}$, $\Delta \mathbf{i}_{r4}$, and $\Delta \mathbf{i}_r^*$, respectively. U_{dc3} and U_{dc4} represent transient response characteristics of the DC voltage loop and their amplitudes are related to all of the transient components in the rotor current.

Equation (21) shows that the DC bus voltage contains complicated frequency components. To elaborate proportions of frequency components in ΔU_{dc} and their relationships with rotor current, a group of data concerning coefficient amplitudes and time constants of the damping components of rotor current and DC bus voltage is given in Table 1. The parameters used in the calculation are from the simulation case. The voltage at the generator terminal dropped to 70% U_n . Before the fault, the DFIG-WT was operated at a rated active power and with a unit power factor.

Table 1. Coefficient amplitudes and time constants of attenuation components in i_r and ΔU_{dc} .

i_r Coefficient Amplitude/p.u.	ΔU_{dc} Coefficient Amplitude/p.u.	Attenuation Time Constant	
Δi_{r1}	0.7026	U_{dc1} 0.1351	τ_s 0.0306
Δi_{r2}	0.0316	U_{dc2} 0.0009	τ_i 0.0575
Δi_{r3}	0.2112	U_{dc3} 0.0312	$1/\omega_{ci}$ 0.0019
Δi_{r4}	0.2275	U_{dc4} 0.0410	$1/\omega_{ci}$ 0.0019
Δi_r^*	0.3332	U_{dc5} 0.0369	$1/\omega_{ci}$ 0.0019
		U_{dc6} 0.0505	$-1/\lambda_1$ 0.0079
		U_{dc7} 0.0579	$-1/\lambda_2$ 0.004

The following conclusions can be drawn from Table 1:

- (1) Fundamental frequency attenuation components Δi_{r1} and U_{dc1} account for the highest proportion in rotor current and DC bus voltage, respectively.
- (2) DC attenuation components Δi_{r2} and U_{dc2} account for the lowest proportion.
- (3) In rotor current, oscillating attenuation components Δi_{r3} and Δi_{r4} , of which both frequencies and time constants are ω_{ci} , will cause the homogeneous components U_{dc3} and U_{dc4} in DC bus voltage. Due to the high switching frequency of RSC, U_{dc3} and U_{dc4} attenuate very quickly. They will attenuate to lower than 10% of their amplitude by about 4 ms.
- (4) U_{dc6} and U_{dc7} in DC bus voltage are related to the characteristic roots of the transfer function of the DC voltage loop. According to Equation (10), the characteristic roots are related to the intermediate frequency bandwidth of the DC voltage loop. When $\omega_{cv} < 7$, the characteristic roots of the transfer function are a pair of conjugate complexes. Under this circumstance, U_{dc6} and U_{dc7} are oscillating attenuation components. The oscillation period is the imaginary part of the characteristic roots, and the attenuation time constant is the reciprocal of the real part of the characteristic roots. When $\omega_{cv} \geq 7$, the characteristic roots are two different (or same) real numbers. In this case, U_{dc6} and U_{dc7} are DC attenuation amplitudes, and the attenuation time constant is the reciprocal of the characteristic roots.

4.2. GSC Current

Equation (21) is transferred into the frequency domain and then substituted into Equation (8). The expression of GSC current in the synchronous reference frame is:

$$\begin{aligned} i_g = & -s i_{sd}^* + j i_{sq}^* + \frac{U_{dc1} K_{vI}}{r} [I_{g1} \cos(\omega t) + I_{g2} \sin(\omega t)] e^{-t/\tau_s} + \frac{U_{dc2} \tau_i}{\tau_i - \tau_v} (K_{vP} - \tau_i K_{vI}) e^{-t/\tau_i} + \frac{U_{dc5}}{1 - \omega_{ci} \tau_v} (K_{vP} - \frac{1}{\omega_{ci}} K_{vI}) e^{-\omega_{ci} t} \\ & + \frac{U_{dc6}}{1 + \lambda_1 \tau_v} (K_{vP} + \frac{1}{\lambda_1} K_{vI}) e^{\lambda_1 t} + \frac{U_{dc7}}{1 + \lambda_2 \tau_v} (K_{vP} + \frac{1}{\lambda_2} K_{vI}) e^{\lambda_2 t} + K_{vI} [I_{g3} \sin(\omega_{ci} t) + I_{g4} \cos(\omega_{ci} t)] e^{-\omega_{ci} t} + I_{g5} (K_{vP} - \tau_v K_{vI}) e^{-t/\tau_v} \end{aligned} \quad (22)$$

where I_{g1} , I_{g2} , I_{g3} , I_{g4} , and I_{g5} are coefficients for different components. Specific expressions are shown in Appendix B.

Comparing Equations (21) and (22), GSC current in the synchronous reference frame contains frequency components corresponding to the transient attenuation components in U_{dc} and additionally generates a DC attenuation component with time constant τ_v due to the inner current loop. According to Table 1, U_{dc2} has a small amplitude, and U_{dc3} , U_{dc4} , and U_{dc5} attenuate quickly. Therefore, it is

applicable to neglect the above parameters to obtain a simplified expression of GSC current. Transferred into the stationary reference frame, the a-phase expression of GSC current is:

$$i_{ga} \approx -s i_{sdf} \cos(\omega t) - i_{gq}^* \sin(\omega t) + [I_{g5}(K_{vP} - \tau_v K_{vI})e^{-t/\tau_v} + \frac{U_{dc6}}{1+\lambda_1\tau_v}(K_{vP} + \frac{1}{\lambda_1}K_{vI})e^{\lambda_1 t} + \frac{U_{dc7}}{1+\lambda_2\tau_v}(K_{vP} + \frac{1}{\lambda_2}K_{vI})e^{\lambda_2 t}] \cos(\omega t) + \frac{U_{dc1}K_{vI}}{2r} [I_{g1} \cos(2\omega t) + I_{g2} \sin(2\omega t)]e^{-t/\tau_s} + \frac{U_{dc1}K_{vI}}{2r} I_{g1} e^{-t/\tau_s} \quad (23)$$

Equation (23) demonstrates that GSC current in the stationary reference frame contains a steady-state fundamental component, a fundamental component attenuating at different time constants, a DC attenuation component, and a second harmonic frequency attenuation component. Among them, the amplitude of the second harmonic frequency attenuation component is proportional to the fundamental attenuation component in DC bus voltage. According to Table 1, it can be deduced that the second harmonic frequency attenuation component accounts for a large proportion of GSC transient current and takes four to six periods to damp to 0. This second component will influence the second harmonic restraint of transformer protection, which will be further discussed in the simulation section.

4.3. Stator Current and DFIG-WT Total Current

According to Equations (1), (17), and (20), the time domain expression of stator current in the synchronous reference frame is:

$$i_s = L_{es} \{ -i_r^* - jU_{s1}/L_m - (\Delta i_{r1} + j\Delta U_s/L_m)e^{-j\omega_1 t} e^{-t/\tau_s} - \Delta i_{r2} e^{-t/\tau_i} - [\Delta i_{r3} \cos(\omega_{ci} t) + \Delta i_{r4} \sin(\omega_{ci} t) + \Delta i_r^*] e^{-\omega_{ci} t} \} \quad (24)$$

where $L_{es} = L_m/L_s$.

Transferring Equation (24) to the stationary reference frame, the a-phase stator current expression is:

$$i_{sa} = \text{Re} \left\{ -L_{es} i_r^* e^{j\omega_1 t} - jL_{es} U_{s1}/L_m e^{j\omega_1 t} - L_{es} (\Delta i_{r1} + j\Delta U_s/L_m) e^{-t/\tau_s} - L_{es} \Delta i_{r2} e^{j\omega_1 t} e^{-t/\tau_i} - L_{es} [\Delta i_{r3} \cos(\omega_{ci} t) + \Delta i_{r4} \sin(\omega_{ci} t) + \Delta i_r^*] e^{j\omega_1 t} e^{-\omega_{ci} t} \right\} \quad (25)$$

Equation (25) reveals that the a-phase stator short-circuit current contains a steady-state fundamental component, a fundamental attenuation component, a DC attenuation component, and an oscillating attenuation component with ω_{ci} as the period and time constant. It can be concluded from Table 1 that the transient attenuation component of the stator current mainly contains a DC attenuation component, while fundamental attenuation and ω_{ci} relevant components account for a small proportion and attenuate quickly.

With the above analysis and deduction, a short-circuit total current calculation model of DFIG-WT can finally be built as the sum of GSC current and stator current according to Equations (22) and (24):

$$i_T = i_s + i_g \quad (26)$$

To demonstrate the transient short-circuit current calculation model of DFIG-WT effectively, a simplified diagram of the relations among key electrical quantities based on the structure of DFIG-WT is shown in Figure 3a, and a detailed flow chart of the entire derivation process is presented in Figure 3b. In the figure, the symbol in bold represents complex vectors in the two phase synchronous rotation coordinate system, and the normal form represents the d (or q)-axis component.

According to Figure 3, the construction process of the transient short circuit current calculation model of DFIG-WT is summarized as follows:

At first, the terminal voltage of DFIG-WT drops to u_{s1} , causing a fundamental frequency attenuation component (ψ_{sn}) that appears in the stator flux, and at the same time, making changes to the reference value of RSC current (i_r^*). The fundamental frequency attenuation component in the stator flux creates a voltage disturbance quantity (e_r) in the current inner loop of RSC, which causes

transient fluctuation of the rotor current (Δi_{r-er}), and change of the reference value of RSC current will also cause a transient component in the rotor current. The above two transient components, together with the steady-state component determined by the reference value of the rotor current, constitute the post-fault rotor current. At last, the calculation model of stator short circuit current can be built according to the rotor current and stator flux.

Meanwhile, the rotor current is converted to the DC side of converters as load current (i_L) of the GSC. According to the control diagram of the voltage outer loop of the GSC, changes of load current (Δi_L) will cause a fluctuation component (ΔU_{dc}) in DC bus voltage, causing further fluctuation of the d-axis component of GSC current. The q-axis component of GSC current is generally 0 or very small, which can be considered as equal to its reference value. Finally, the transient short circuit current calculation model of DFIG-WT is the sum of the stator current and GSC current.

According to the above analysis and the flow chart, the generating mechanism and evolution law of transient fluctuations of critical electrical quantities of the DFIG-WT are revealed clearly.

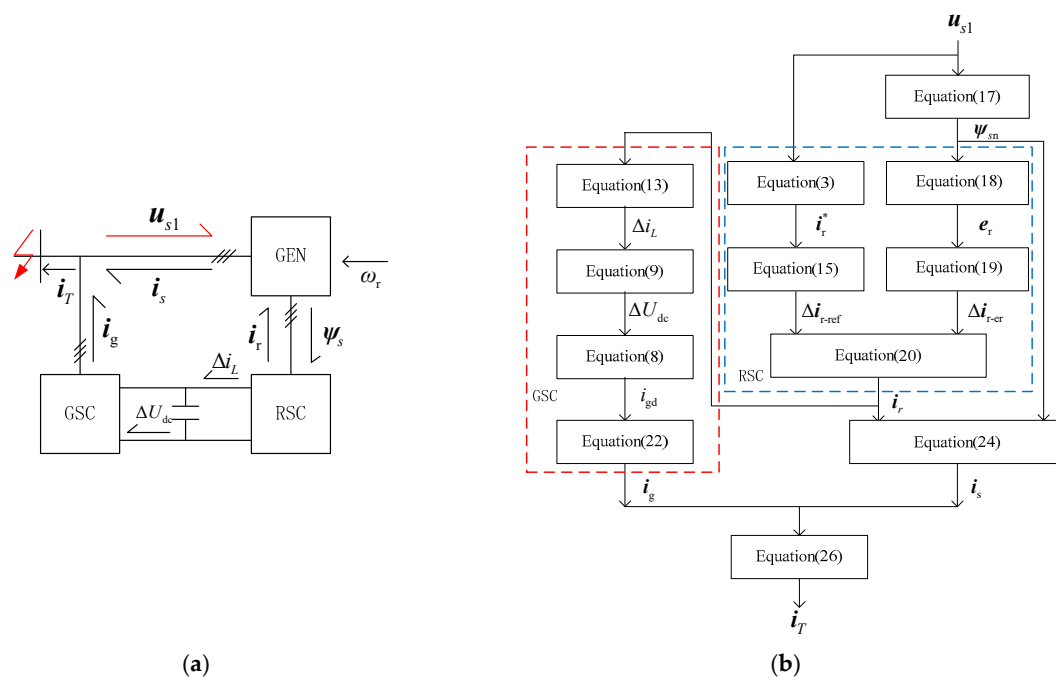


Figure 3. Flow chart of the integration process of the transient short-circuit current calculation model for DFIG-WT: (a) simplified graphic of the relations among critical quantities; (b) detailed flow chart of the integration process.

4.4. Analysis of Steady-State Current of DFIG-WT Considering Current Limits

With a detailed short-circuit current calculation model, quantitative analysis can be carried out to further reveal the fault characteristics of DFIG-WT. Among all the frequency components of the SCC, fundamental components are the most important to protection settings. As shown in Equations (22) and (24), fundamental components of total SCC are mainly composed of steady-state components, while the transient fundamental components attenuate rapidly. Therefore, a detailed analysis of the steady-state current of DFIG-WT was carried out considering the current limit.

According to Equations (22) and (24), the complex of the steady-state component is:

$$i_{Tf} = -\omega_r \frac{L_m}{L_s} i_{rd1}^* - j \left(\frac{U_{s1}}{L_s} + \frac{L_m}{L_s} i_{rq1}^* + i_{gq}^* \right) \quad (27)$$

According to Equation (4) and considering the limit of the converter, the q-axis component of the rotor reference current linearly increases as the voltage drop deepens, while the d-axis component

is double-limited by the maximum load current and the maximum rotor current. With parameters from the simulation case, three-dimensional diagrams and contour maps concerning the d-axis rotor reference current and the amplitude of the steady-state short-circuit current of DFIG-WT (I_{Tf}) are shown in Figure 4. The x-axis is the amplitude of post-fault voltage U_{s1} and the y-axis is the pre-fault stator active power P_{s0} .

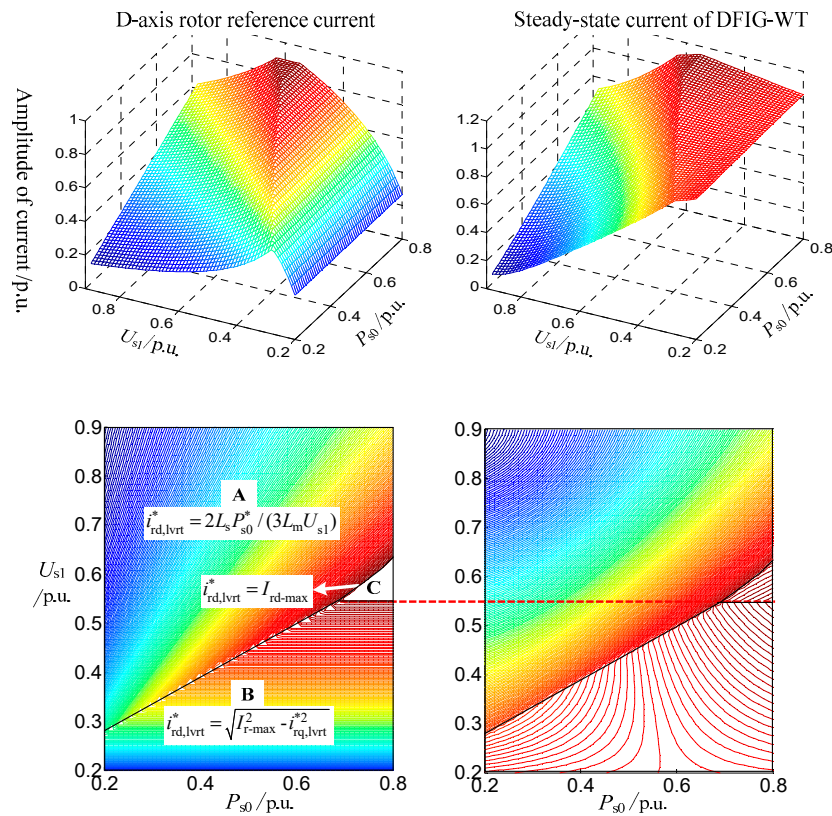


Figure 4. Characteristics of steady-state components of DFIG-WT fault current.

It can be seen from Figure 4 that, due to the influence of current-limiting of the converter, the steady-state short-circuit current of DFIG-WT exhibits nonlinearity when the terminal post-fault voltages and pre-fault power change. It is worth noticing that the deeper the voltage sag is, the larger the steady-state short-circuit current will be. The DFIG steady-state short-circuit current reaches its maximum value when the terminal voltage drops to U_{s-max} and the pre-fault power is full.

According to the contour map of Figure 4, the maximum steady-state short-circuit current of the DFIG appears on the isobaric line between region B and region C of the d-axis rotor reference current. U_{s-max} can be deduced from the boundary of region B and region C:

$$U_{s-max} = \frac{0.9K_d - \sqrt{I_{r-max}^2 - I_{rd-max}^2}}{K_d - 1/L_m} \tag{28}$$

As can be seen from the above equation, U_{s-max} only relates to the RSC reference current limit and reactive current coefficient.

Combining Equations (27) and (28) and ignoring the term $1/L_m$ in the denominator of Equation (28), the estimation formula for the maximum steady-state short-circuit current of DFIG I_{T-max} under different voltage drops and pre-fault conditions is simplified and obtained as:

$$I_{T-max} \approx \sqrt{I_{r-max}^2 + [(\omega_{rmax} \frac{L_m}{L_s})^2 - 1] I_{rd-max}^2} \tag{29}$$

where ω_{rmax} is the maximum rotor speed frequency in per-unit value, usually about 1.2–1.3.

Parameters in the simulation case are used to verify the accuracy of Equation (29). When the DFIG steady-state short-circuit current reaches its maximum, U_{s-max} is about 0.55 p.u. and calculated I_{T-max} is 1.2263 p.u. Compared with the simulation result, the error of the maximum steady-state short-circuit current estimation formula is:

$$\varepsilon = \frac{1.2263 - 1.1821}{1.1821} \times 100\% \approx 3.74\% \quad (30)$$

The estimated value is slightly larger than the actual value, and the error comes from ignoring the term $1/L_m$, which results in the U_{s-max} calculated value decreasing and the short-circuit current reactive current increasing, leading to an increase in the I_{T-max} calculated value. However, due to the excitation inductance, $1/L_m$ is generally large, and the error caused by ignoring this item is small.

According to Equation (30), because of converter current limiting, the steady-state short-circuit current provided by the DFIG-WT is relatively small and has nonlinear relationships with terminal voltage and pre-fault power. This is quite different from the synchronous generators, whose short-circuit current calculation model is a constant internal voltage behind a linear transient impedance, which could bring new problems to the traditional relay setting calculation.

5. Simulation Analysis and Verification

To verify the accuracy of the constructed short-circuit current calculation model and the transient response characteristics of converters during a fault, a simulation system of DFIG-WT with an LVRT control strategy was built in the MATLAB/Simulink simulation platform based on the demo for detailed DFIG-WT. The simulation system is shown in Figure 5. Major parameters of the system are listed in Table 2.

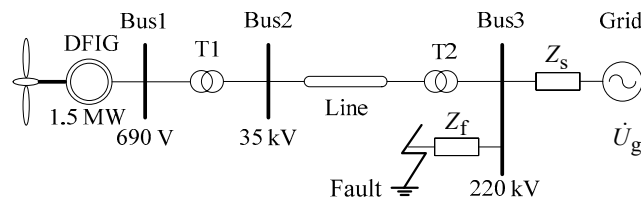


Figure 5. Simulation system.

Table 2. Parameters of the DFIG-WT simulation model.

Parameter	Value	Parameter	Value
Rated capacity	1.5 MW	Switching frequency of RSC	1.6 kHz
Rated voltage of stator	690 V	Proportionality coefficient of inner current loop	0.578
Stator resistance	0.023 p.u.	Integral coefficient of inner current loop	10.58
Rotor resistance	0.016 p.u.	Switching frequency of GSC	2.7 kHz
Stator inductance	3.08 p.u.	Proportionality coefficient of DC voltage loop	6.17
Rotor inductance	3.06 p.u.	Integral coefficient of DC voltage loop	400
Rated DC bus voltage	1150 V	Reactive current coefficient K_d	1.5
Active current-limiting of rotor	0.9 p.u.	Maximum current-limiting value of rotor	1.15 p.u.
DC bus capacitor	0.0032 p.u.	Modulation coefficient of PWM	0.95

5.1. Contrast Verification of Key Electrical Quantities of Generator and Converter

In this simulation case, DFIG-WT operates at a supersynchronous state with a unit power factor when a three-phase-to-ground fault through transition resistance Z_f occurs on Bus 3 at 0.113 s, making the voltage at the generator terminal drop to 0.65 p.u. Before the fault, the stator active power is about 0.82 p.u. and GSC active power is about 0.18 p.u. The slip ratio is about -0.21 .

5.1.1. Verification of DC Bus Voltage

The postfault DC bus voltage was calculated according to Equation (21) and compared with the simulation waveform under the fault condition. According to Equation (4) and the analysis in Section 3.1, when the voltage at the generator terminal drops suddenly, there will be transient fluctuation in U_{dc} , which is caused by the power imbalance of the converters at the two sides. As shown in Figure 6a, the calculated waveform coincides with the simulated waveform, verifying the accuracy of Equation (21).

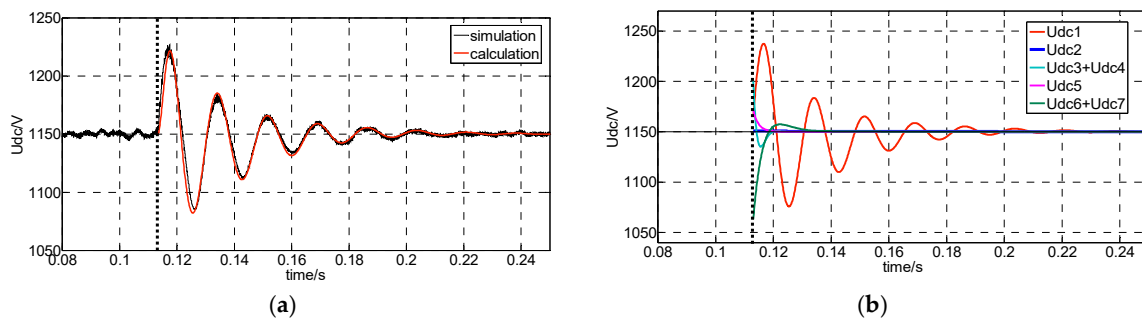


Figure 6. Comparison of DC bus voltage and decomposition of frequency components: (a) comparison between simulated and calculated waveform; (b) decomposition of frequency components.

The decomposition of transient attenuation components in U_{dc} , which are calculated from Equation (21), is shown in Figure 6b. Different frequency components are represented by different colors and their relevant coefficients. As shown in Figure 6b, the fundamental component takes the dominant role among all attenuation components of U_{dc} . The remaining components attenuate to 0 in less than one period and their amplitudes are smaller than the fundamental component.

5.1.2. Verification of GSC Current

A-phase GSC current is calculated according to Equation (23) and is compared with the simulated waveform, as shown in Figure 7a. Under the simulation condition, the peak value of the GSC A-phase short-circuit current is about 0.39 p.u., and generally damps to the steady-state value of 0.16 p.u. in about four periods. The theoretical calculation accurately coincides with simulation results.

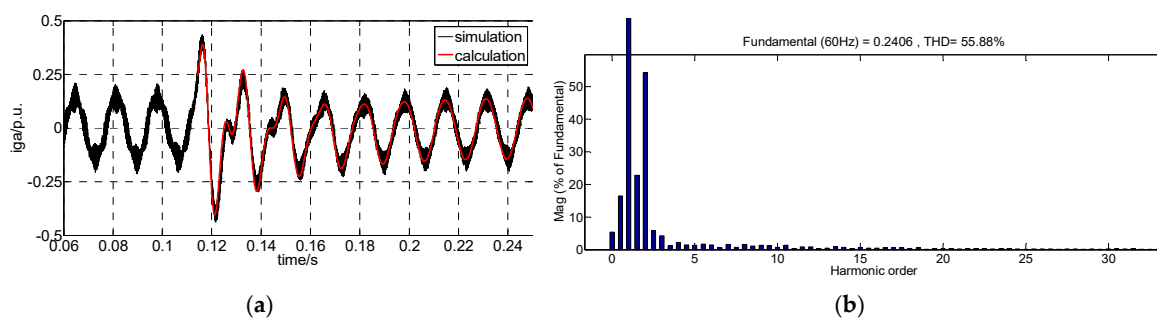


Figure 7. GSC short-circuit current and its frequency spectral analysis: (a) comparison between simulated and calculated waveform; (b) frequency spectral analysis.

It can be observed from Figure 7a that there are evident harmonic components in the first three cycles. The frequency spectral analysis result of the first cycle of simulated A-phase GSC current is shown in Figure 7b. The total harmonic distortion (THD) of the current of the selected window is about 55.88%, and the second harmonic content is about 54.2%. According to the theoretical analysis in Section 4, the fundamental attenuation component, which accounts for a high proportion in DC bus voltage, will induce the second harmonic frequency component in the GSC current. The simulation results coincide with the theoretical analysis.

The characteristics of the second harmonic component in the GSC current are studied further under supersynchronous and subsynchronous conditions. The second harmonic frequency component in GSC is positively related to the voltage dip level according to Equation (23), meaning that a lower residual voltage will cause a higher proportion of the second harmonic component in the short-circuit current. When the terminal voltage drops to 40% U_n , the proportions of the second harmonic component in the short-circuit current of DFIG-WT and GSC are as shown in Figure 8. Moreover, the proportion gets higher under subsynchronous conditions, with up to 68.4% in GSC current and 26.6% in DFIG-WT current.

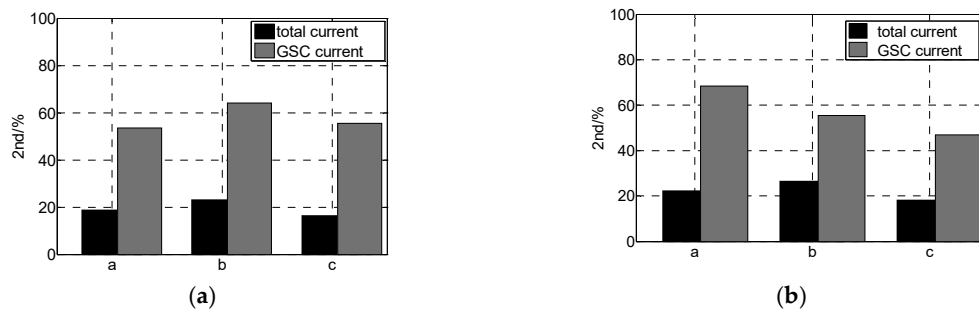


Figure 8. Proportions of the second harmonic component in short-circuit current of DFIG-WT and GSC: (a) supersynchronous, $s = -0.2$; (b) subsynchronous, $s = 0.2$.

Since the method of second harmonic restraint is widely used in transformer protection to overcome maloperation caused by a magnetizing inrush current, and the threshold for second harmonic content is usually set at 15–20%, the high proportion of the second harmonic component generated by DFIG-WT may cause the transformer protection failure to operate.

5.1.3. Verification of Rotor Current

A-phase rotor current was calculated according to Equation (20) and transferred to the rotor coordinate system. A comparison between the calculated waveform and simulated waveform is shown in Figure 9a. According to Equation (19) and Table 1, the fundamental component Δi_{r1} is the key attenuation component of rotor short-circuit current in the synchronous reference frame, while in the rotor coordinate system, its frequency is $(1 - s)$ times the rotor fundamental frequency. In this simulation case, with a slip ratio of -0.21 , the frequency of Δi_{r1} is about 72 Hz and it attenuates to 0 by about 0.064 s.

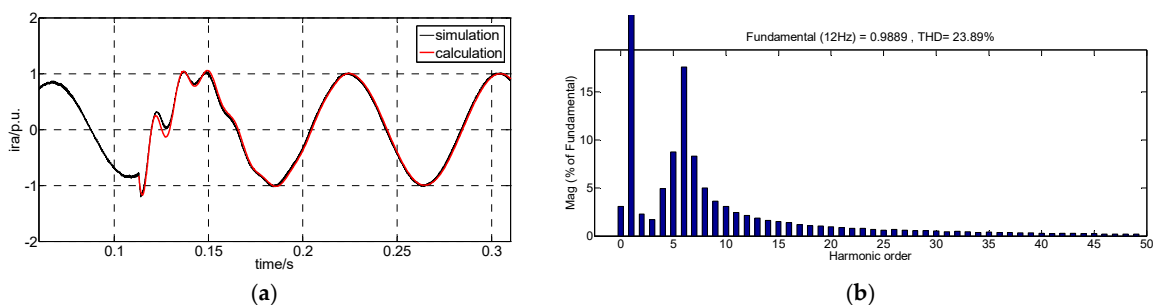


Figure 9. Rotor short-circuit current and its frequency spectral analysis: (a) comparison between simulated and calculated waveform; (b) frequency spectral analysis.

Frequency spectral analysis results of the first cycle of simulated rotor current are shown in Figure 9b. It can be seen from Figure 9b that among different harmonic components, the sixth harmonic accounts for the largest proportion, which is 72 Hz, with a fundamental of 12 Hz. Its proportion relative to the fundamental wave is 17.6%. Besides, as discussed in Section 3.2, there is no sudden change of rotor current at the moment the fault happens because the calculation considers the sampling

delay and PWM small inertial characteristics. Theoretical analysis coincides with simulation results, which verifies the accuracy of the theory.

5.1.4. Verification of Stator Current

A comparison between the A-phase stator current calculated by Equation (25) and the simulated waveform is shown in Figure 10. When the voltage at the generator terminal drops to 0.65 p.u., the peak value of A-phase stator short-circuit current is about 1.37 p.u. and the steady-state value is about 0.81 p.u. According to Equation (25) and as shown in Figure 10b, DC is the main transient attenuation component of the stator short-circuit current.

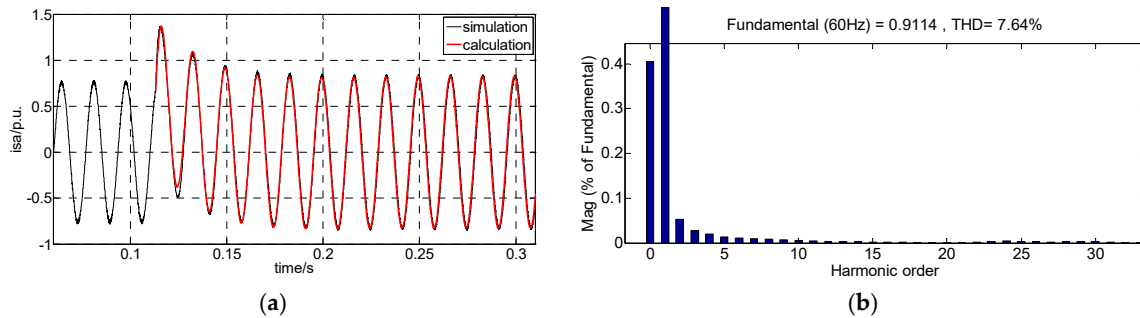


Figure 10. Stator short-circuit current and its frequency spectral analysis: (a) comparison between simulated and calculated waveform; (b) frequency spectral analysis.

Compared with Figure 7, the short-circuit current of GSC is about 20% of the stator short-circuit current in a steady state, while the peak value of GSC SCC is about 28.5% of the stator SCC. In [15–17], the GSC current is neglected and the stator current is used to replace the short-circuit total current of DFIG-WT, which will surely result in a large calculation error.

5.2. Contrast Verification of DFIG-WT Transient Characteristics under Different Situations

For a more comprehensive analysis and verification of the theoretical analysis, 15 groups of experiments were carried out under different operating conditions and voltage drops. A comparison between simulated results and calculated results of key characteristic parameters of the short-circuit current is shown in Figure 11, with solid lines representing simulation results and dotted lines representing calculated results.

In the experiments, three typical working conditions of DFIG-WT were chosen: supersynchronous ($s = -0.2$), synchronous ($s = 0.01$), and subsynchronous ($s = 0.2$). The voltage at the generator terminal dropped to 0.35 p.u., 0.47 p.u., 0.6 p.u., 0.75 p.u., and 0.9 p.u., respectively. Key characteristic parameters include peak values of DFIG-SCC and stator SCC, and steady-state values of DFIG-SCC and GSC-SCC.

The diagrams in the first row of Figure 11 show variations of the four key characteristic parameters with different residual voltages and operating conditions. Under the supersynchronous condition, the peak value of total current is higher than that of stator current. However, the opposite phenomenon is observed under the subsynchronous condition, while under the synchronous condition, these two parameters are almost equal to each other. This is because GSC current has the same direction as stator current under the supersynchronous condition, the opposite direction under the subsynchronous condition, and almost 0 under the synchronous condition.

The diagrams in the second row of Figure 11 show steady-state value proportions of GSC-SCC of DFIG-SCC. Under the subsynchronous condition, the proportion of GSC current is higher than that in other conditions, reaching 35% at the most.

Among the comparisons in all cases, the maximum calculation error is about 6.8%, as shown in Figure 11, which occurred at the peak value of DFIG-SCC when $s = -0.2$ and the voltage dropped to 0.35 p.u.

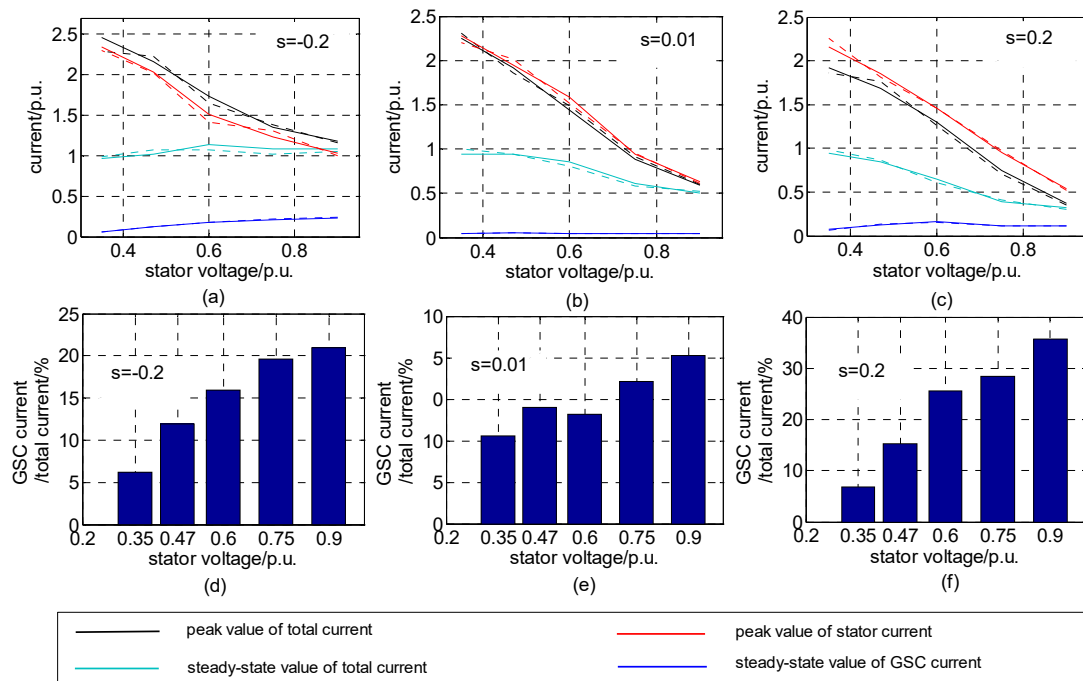


Figure 11. Contrast verification of key characteristic parameters of short-circuit current under different conditions, as well as proportions of steady-state GSC-SCC.

6. Verification with LVRT Test Data

According to the grid criteria for wind power [27], the LVRT test must be conducted with all kinds of wind turbines before they have access to the grid, which provides reference data for studying the fault characteristics of wind turbine generators. The LVRT test schematic diagram is shown in Figure 12a. A movable vehicle-mounted container structure is adopted by LVRT test devices, including a voltage sag generator and remote console cabinet, as shown in Figure 12b. The terminal voltage of tested wind turbines is remotely controlled by adjusting the voltage division ratio of the current, limiting reactance, and short-circuit reactance. The three-phase voltage and current at the terminal of tested wind turbines are saved by a Dewetron DEWE-5000 high-precision recorder (DEWETRON, Grambach, Austria).

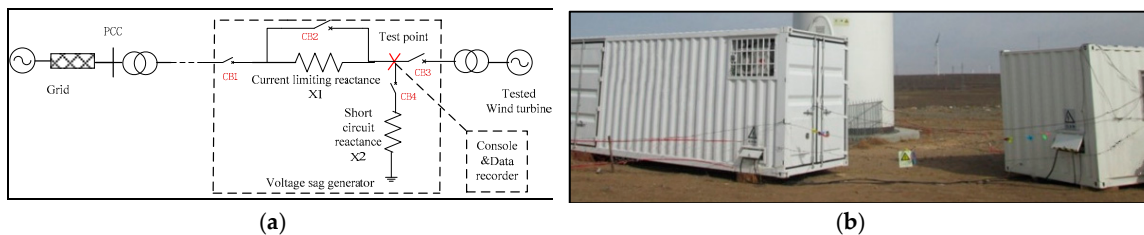


Figure 12. (a) LVRT test schematic diagram, (b) picture of the LVRT field test devices.

In the following section, a group of field test data are analyzed and compared with the proposed analytic expressions. Parameters of the tested DFIG-WT are listed in Table 3. In the test, the terminal voltage dropped to about 0.23 p.u. under subsynchronous ($P = 0.28$ p.u., $s = 0.2$) and supersynchronous ($P = 0.97$ p.u., $s = -0.2$) conditions.

Table 3. Parameters of the tested DFIG-WT.

Parameter	Value	Parameter	Value
Rated capacity	1.5 MW	Leakage inductance of rotor	0.0162 Ω
Rated voltage of stator	690 V	Exciting inductance	1.123 Ω
Rated voltage of rotor	1800 V	Switching frequency of converter	2.5 kHz
Stator resistance	0.0023 Ω	Current-limiting value of rotor	1.5 p.u.
Rotor resistance	0.0024 Ω	Reactive current coefficient	1.8
Leakage inductance of stator	0.0184 Ω	Rated voltage of DC bus	1150 V
Proportionality coefficient of inner current loop	0.6	Proportionality coefficient of DC voltage loop	10
Integral coefficient of inner current loop	15	Integral coefficient of DC voltage loop	500
DC bus capacitor	0.001 F	Modulation coefficient of PWM	0.95

Active and reactive power generated by wind turbines under two test conditions are shown in Figure 13. As the grid codes require, wind power generators should output reactive power during the LVRT process to support grid voltage recovery. It can be concluded from Equation (3) that active power during the LVRT process under different operating conditions should be the same with the same voltage dip level. As shown in Figure 13, the reactive power is about 0.3 p.u. under both test conditions during the LVRT process as the residual voltages are the same. Reactive power output is the primary concern for DFIG-WT control, limiting the active power output capacity. The active power in the supersynchronous condition (about 0.21 p.u.) is slightly larger than that in the subsynchronous condition (about 0.14 p.u.). This is because GSC outputs active power under the supersynchronous condition and absorbs active power under the subsynchronous condition.

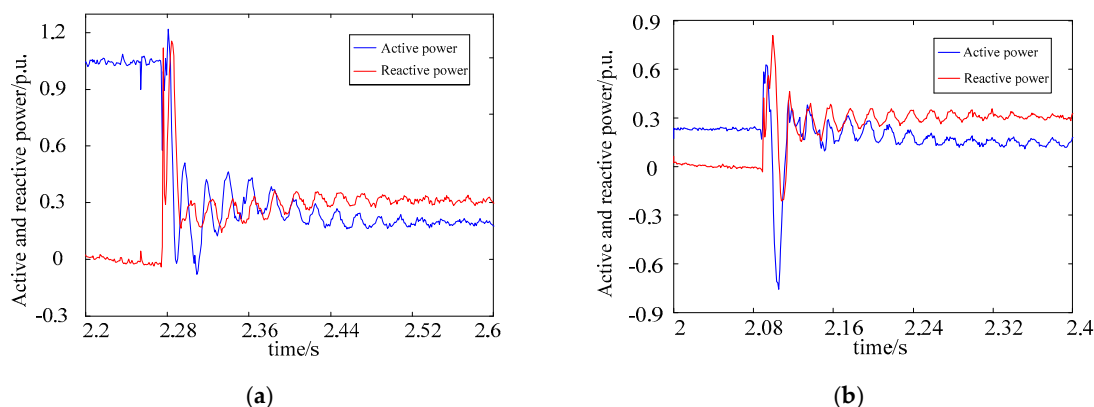


Figure 13. Active and reactive power under different conditions: (a) supersynchronous condition; (b) subsynchronous condition.

Parameters of the tested DFIG-WT are substituted into Equations (21), (24), and (26) to obtain the calculated waveforms of the DFIG-SCC under different conditions. A comparison between the actual waveforms and calculated waveforms is shown in Figure 14. Transient characteristics and the attenuation law of the calculated waveform and simulated waveform are consistent. However, the first three circles do not match well. This is because the controller may not be able to perform as ideally as the simulated model under severe fault conditions. Moreover, the steady-state short-circuit current agrees precisely.

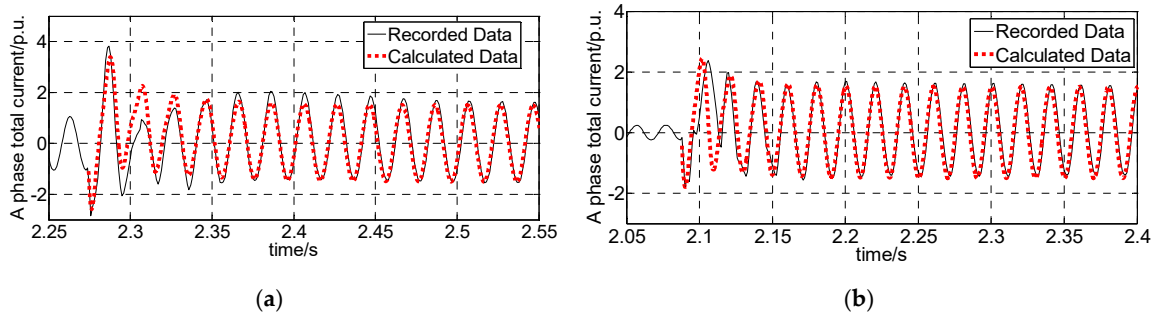


Figure 14. Comparison between recorded data and calculated data under two operating conditions: (a) supersynchronous condition; (b) subsynchronous condition.

According to the test data, the steady-state value of the short-circuit current is 1.642 p.u. under the supersynchronous condition and 1.507 p.u. under the subsynchronous condition. Parameters of DFIG-WT are transferred into per-unit values and substituted into Equation (3). The reference values of rotor current are gained as:

$$\begin{cases} i_{rq,lvrt}^* = -[1.8 \times (0.9 - 0.23)] \times \frac{3.5961}{3.5381} - \frac{0.23}{3.5961} = -1.2908 \\ i_{rd,lvrt}^* = \sqrt{1.5^2 - i_{rq,lvrt}^{*2}} = 0.7641 \end{cases} \quad (31)$$

The reference values of rotor current are substituted into Equation (26). The steady-state short-circuit current under the two conditions is calculated as:

$$\begin{cases} I_{Tf-full} = \left| -1.2 \times \frac{3.5381}{3.5961} \times i_{rd,lvrt}^* - j\left(\frac{0.23}{3.5961} - i_{rq,lvrt}^*\right) \right| \\ = |-0.9021 - j1.3339| = 1.6103 \\ I_{Tf-low} = \left| -0.8 \times \frac{3.5381}{3.5961} \times i_{rd,lvrt}^* - j\left(\frac{0.23}{3.5961} - i_{rq,lvrt}^*\right) \right| \\ = |-0.6041 - j1.3339| = 1.4632 \end{cases} \quad (32)$$

where $I_{Tf-full}$ and I_{Tf-low} are amplitudes of short-circuit currents of DFIG-WT under full and sub synchronous conditions, respectively. Their relative errors with test data are 1.9% and 2.9%, respectively, verifying the accuracy of the proposed analytical expression.

The second harmonic contents of the first cycle in the three-phase short-circuit current under two conditions are shown in Table 4. According to Table 4, the following conclusions can be drawn as follows:

- (1) According to theoretical derivation and Equation (23), the deeper the voltage drops, the higher the second harmonic content will be. It can be seen from Table 4 that when the terminal voltage drops to 0.23 p.u., the second harmonic content in the three-phase short circuit current can reach up to 51.74%, far exceeding the transformer’s second harmonic setting value (15–20%).
- (2) Under the same voltage drop level, the second harmonic content is higher under the sub-synchronous condition than the super-synchronous condition. This is because the secondary harmonics are mainly generated by GSC, and the proportion of GSC current to the total current is higher under the sub-synchronous condition, which is consistent with the result in Figure 8.
- (3) Then second harmonic content in the three-phase current is different, and this phenomenon can be explained by the mechanism of second harmonic generation. According to the theoretical derivation and the flow chart in Figure 4, the second harmonic component in three phase short circuit currents is originally caused by the DC component in stator flux, which is generated due to the conservation law of flux linkage and its amplitude is determined by the instantaneous value of stator flux at the time the fault occurs. Therefore, the DC attenuation components in the three phases are not equal, so that the second harmonic content in three phases is also different.

- (4) The phase with the highest second harmonic content is related to the time of failure due to the same reason at the point (3). In Table 4, the highest second harmonic content is in phase C when the fault occurred at 2.27 s under the super synchronous condition, and it is phase A when the fault occurred at 2.08 s under the sub synchronous condition. As shown in Figure 8, in the simulation study, the fault occurs at the same time in both cases, and the phase with the highest second harmonic content is phase B.

Table 4. Second harmonic contents of three-phase short-circuit current under two conditions.

Operating Condition	A-Phase	B-Phase	C-Phase
Super-synchronous	32.68%	25.16%	43.40%
Subsynchronous	49.45%	34.58%	51.74%

7. Conclusions

In this paper, transient characteristics of DFIG-WT short-circuit current under converter control are analyzed and a detailed analytical calculation model of short-circuit total current of DFIG-WT, including GSC current and stator current, is deduced. Based on the established model, the characteristics of steady-state fault current of DFIG-WT are further studied. The accuracy of the theoretical analysis and mathematical deduction is verified by comparing simulation test and LVRT field test data. The main work of this paper can be summarized and conclusions can be drawn as follows:

- (1) Equations for GSC current, DC bus voltage, and rotor current are constructed. The disturbance evolution mechanism in converters and the coupling relationships of the electrical quantities are thus revealed.
- (2) The transient analytical models of GSC current, DC bus voltage, stator current, and rotor current are constructed. With the transient analytical model, short-circuit current frequency components, key influencing factors, and attenuation characteristics are quantized.
- (3) The amplitude of steady-state short-circuit current of DFIG-WT varies with the post-fault terminal voltage and pre-fault power nonlinearly, considering the multi-limitation of rotor current. Estimation formulas for the maximum steady-state SCC of DFIG-WT and the corresponding voltage are put forward and verified by simulation.
- (4) It is proved by theoretical analysis and simulation that the proportion of short-circuit current of GSC is related to the pre-fault operation state. The proportion of GSC current is higher under subsynchronous conditions. The accurate calculation of the total short-circuit current of DFIG-WT should take the influence of GSC current into account, or it will generate up to 30% error.
- (5) Reasons for high second harmonic contents contained in the transient short-circuit current of GSC are disclosed. It is concluded that the second harmonic content is positively related to the voltage dip level, and the second harmonic component might have an adverse impact on transformer differential current protection.

The results and conclusions in this paper could provide theoretical references for short-circuit current calculation of power systems with DFIG-WTs connected to the grid, as well as optimizing settings and redesigns for relevant protection, such as transformer protection with second harmonic restraint. Moreover, from the aspect of control strategies of converters, if the fluctuation of DC bus voltage could be suppressed, the second harmonic content contained in the short-circuit current should also be decreased.

Author Contributions: Conceptualization, J.L. and T.Z.; methodology, J.L.; software, J.L.; validation, J.L. and T.Z.; formal analysis, J.L.; investigation, J.L.; resources, Z.W.; data curation, J.L.; writing—original draft preparation, J.L.; writing—review and editing, J.L., T.Z. and Z.W.; visualization, J.L.; supervision, T.Z. and Z.W.; project administration, T.Z. and Z.W.; funding acquisition, Z.W.

Funding: This work was funded by the National Key Research and Development Plan of China (2016YFB0900640) and Research Project of State Grid Corporation of China (5211TZ16000F).

Acknowledgments: We acknowledge the North China Electric Power Research Institute (NCEPRI), which provided technical support and LVRT field test data for this research.

Conflicts of Interest: The authors declare no conflict of interest.

Nomenclature

u_s, u_r	Stator and rotor voltage vectors	L_s, L_r	Stator and rotor self-inductances
i_s, i_r	Stator and rotor current vectors	R_s, R_r	Stator and rotor resistances
ψ_s, ψ_r	Stator and rotor flux vectors	L_m	Mutual inductance
i_g	GSC current vector	C	Capacitance of the capacitor
i_T	Total current vector of DFIG-WT	L, R	Filter inductance and resistance
U_{dc}	DC bus voltage	P_g	Active power of the GSC
i_L, i_{g-dc}	DC-side currents of RSC and GSC	$i_{ra,b,c}$	AC-side three-phase rotor currents
P_{load}	DC-side active power of the RSC	*	Superscript donating reference value
ω_1	Synchronous angular frequency	s	Slip of DFIG
U_{s0}, U_{s1}	Amplitudes of pre-fault and post-fault stator voltages	P_{s0}^*, Q_{s0}^*	Reference values of pre-fault stator active and reactive powers
p	Differential operator	S_{abc}	Switch function of the converter
d, q	Subscripts donating d-axis component and q-axis component	f, n	Subscripts donating forced component and natural component

Note: a symbol in bold form denotes a complex vector.

Appendix A

Control diagrams of the RSC and GSC

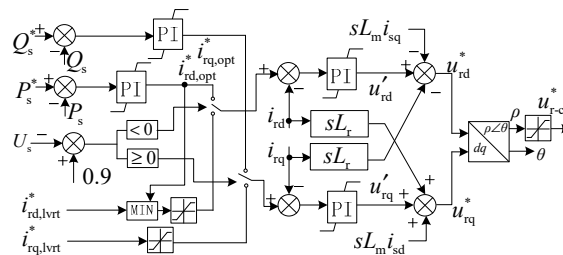


Figure A1. Control diagram of the RSC.

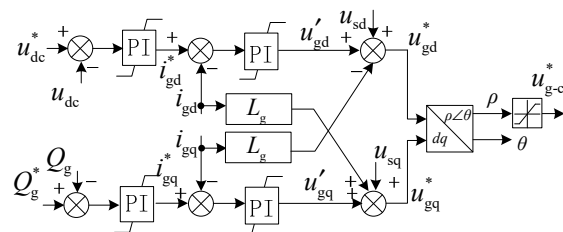


Figure A2. Control diagram of the GSC.

Appendix B

1. Coefficients of rotor current in Equation (19):

$$\Delta i_{r1} = k_0 \frac{2\omega_{ci}k_4 + k_2}{k_1k_4 - k_2k_3} \left(\frac{1}{\tau_s} + j\omega_1 \right)$$

$$\Delta i_{r2} = -k_0 \frac{k_1 + 2\omega_{ci}k_3}{k_1k_4 - k_2k_3} \frac{1}{\tau_i}$$

$$\Delta \mathbf{i}_{r3} = k_0 [2\omega_{ci} (\frac{k_1 + 2\omega_{ci}k_3}{k_1k_4 - k_2k_3} - \frac{2\omega_{ci}k_4 + k_2}{k_1k_4 - k_2k_3}) - k_5]$$

$$\Delta \mathbf{i}_{r4} = k_0k_5$$

where

$$k_0 = -j(\frac{1}{\omega_1\tau_s} + j) \frac{L_m}{sL_s} \frac{\Delta U_s}{3T_s K_{p_i} K_{p_{wm}}}$$

$$k_1 = \frac{1}{\tau_i} [(\omega_{ci} - \frac{1}{\tau_s} - j\omega_1)^2 + \omega_{ci}^2]$$

$$k_2 = (\frac{1}{\tau_s} + j\omega_1) [(\frac{1}{\tau_i} - \omega_{ci})^2 + \omega_{ci}^2]$$

$$k_3 = -\omega_{ci}^2 - [\omega_{ci} - (\frac{1}{\tau_s} + j\omega_1)]^2$$

$$k_4 = -\omega_{ci}^2 - (\omega_{ci} - \frac{1}{\tau_i})^2$$

$$k_5 = \frac{(2\omega_{ci} - \frac{1}{\tau_i})(k_1 + 2\omega_{ci}k_3) - [2\omega_{ci} - (\frac{1}{\tau_s} + j\omega_1)](k_2 + 2\omega_{ci}k_4)}{k_1k_4 - k_2k_3}$$

2. Coefficients of DC bus voltage in Equation (21):

$$U_{dc1} = -0.75m |\Delta \mathbf{i}_{r1}| \frac{\omega_1 a}{Cn}$$

$$U_{dc2} = 0.75m \frac{\omega_1}{C} |\Delta \mathbf{i}_{r2}| \cos(\alpha_2 + \delta) \frac{1/\tau_i}{(R + 1/\tau_i)^2 - M^2}$$

$$U_{dc3} = -0.75m \frac{\omega_1}{C} |\Delta \mathbf{i}_{r3}| \cos(\alpha_3 + \delta) \frac{\sqrt{2}\omega_{ci}}{x}$$

$$U_{dc4} = -0.75m \frac{\omega_1}{C} |\Delta \mathbf{i}_{r4}| \cos(\alpha_4 + \delta) \frac{\sqrt{2}\omega_{ci}}{x}$$

$$U_{dc5} = -0.75m \frac{\omega_1}{C} |\Delta \mathbf{i}_r^*| \cos(\alpha_5 + \delta) [\frac{\omega_{ci}}{(R + \omega_{ci})^2 - M^2}]$$

$$U_{dc6} = \frac{1}{2M} [U_{dc1} \frac{n}{a} \frac{\lambda_1 \cos(\alpha_1 + \delta - \theta_4)}{\sqrt{(\lambda_1 + 1/\tau_s)^2 + \omega^2}} + U_{dc2} \frac{(R + 1/\tau_i)^2 - M^2}{1/\tau_i} \frac{\lambda_1}{\lambda_1 + 1/\tau_i}$$

$$+ U_{dc3} \frac{x}{\sqrt{2}\omega_{ci}} \frac{\lambda_1 + \omega_{ci}}{(\lambda_1 + \omega_{ci})^2 + (\omega_{ci})^2} + U_{dc4} \frac{x}{\sqrt{2}} \frac{\lambda_1}{(\lambda_1 + \omega_{ci})^2 + (\omega_{ci})^2} + U_{dc5} \frac{(R + \omega_{ci})^2 - M^2}{\lambda_1 + \omega_{ci}}]$$

$$U_{dc7} = -\frac{1}{2M} [U_{dc1} \frac{n}{a} \frac{\lambda_2 \cos(\alpha_1 + \delta - \theta_5)}{\sqrt{(\lambda_2 + 1/\tau_s)^2 + \omega^2}} + U_{dc2} \frac{(R + 1/\tau_i)^2 - M^2}{1/\tau_i} \frac{\lambda_2}{\lambda_2 + 1/\tau_i}$$

$$+ U_{dc3} \frac{x}{\sqrt{2}\omega_{ci}} \frac{\lambda_2 + \omega_{ci}}{(\lambda_2 + \omega_{ci})^2 + (\omega_{ci})^2} + U_{dc4} \frac{x}{\sqrt{2}} \frac{\lambda_2}{(\lambda_2 + \omega_{ci})^2 + (\omega_{ci})^2} + U_{dc5} \frac{(R + \omega_{ci})^2 - M^2}{\lambda_2 + \omega_{ci}}]$$

where $\lambda_{1,2} = R \pm M$,

$$\alpha_1 = a \tan \frac{\text{Re}[\Delta \mathbf{i}_{r1}]}{\text{Im}[\Delta \mathbf{i}_{r1}]}, \alpha_2 = a \tan \frac{\text{Re}[\Delta \mathbf{i}_{r2}]}{\text{Im}[\Delta \mathbf{i}_{r2}]}, \alpha_3 = a \tan \frac{\text{Re}[\Delta \mathbf{i}_{r3}]}{\text{Im}[\Delta \mathbf{i}_{r3}]}, \alpha_4 = a \tan \frac{\text{Re}[\Delta \mathbf{i}_{r4}]}{\text{Im}[\Delta \mathbf{i}_{r4}]}, \alpha_5 = a \tan \frac{\text{Re}[\Delta \mathbf{i}_r^*]}{\text{Im}[\Delta \mathbf{i}_r^*]}$$

$$ae^{j\theta_1} = 1/\tau_s + j\omega$$

$$ne^{j\theta_2} = (R + 1/\tau_s)^2 - \omega^2 + M^2 + 2j\omega(R + 1/\tau_s)$$

$$xe^{j\theta_3} = (R + 1/3T_s + j/3T_s)^2 + M^2$$

$$\theta_4 = a \tan \frac{\omega_1}{\lambda_1 + 1/\tau_s}$$

$$\theta_5 = a \tan \frac{\omega_1}{\lambda_2 + 1/\tau_s}$$

$$\beta_1 = \alpha_1 + \delta + \theta_1 - \theta_2$$

$$\beta_2 = \theta_3 - \frac{\pi}{4}$$

3. Coefficient of GSC current in Equation (22):

$$I_{g1} = \left(\omega_{cv} - \frac{1}{a^2 \tau_v \tau_s}\right) \cos \beta_1 - \frac{\omega}{a^2 \tau_v} \sin \beta_1$$

$$I_{g2} = \left(\omega_{cv} - \frac{1}{a^2 \tau_v \tau_s}\right) \sin \beta_1 + \frac{\omega}{a^2 \tau_v} \cos \beta_1$$

$$I_{g3} = U_{dc3} \left(\cos \beta_2 - \frac{\cos \beta_2 - \sin \beta_2}{2\omega_{ci}^2 \tau_v}\right) - U_{dc4} \left(\sin \beta_2 - \frac{\sin \beta_2 - \cos \beta_2}{2\omega_{ci}^2 \tau_v}\right)$$

$$I_{g4} = U_{dc3} \left(\sin \beta_2 - \frac{\sin \beta_2 + \cos \beta_2}{2\omega_{ci}^2 \tau_v}\right) - U_{dc4} \left(\cos \beta_2 - \frac{\cos \beta_2 + \sin \beta_2}{2\omega_{ci}^2 \tau_v}\right)$$

$$I_{g5} = -\frac{U_{dc1}}{\tau_v} \left[\frac{\cos \beta_1 (1/\tau_v - 1/\tau_s) - \omega \sin \beta_1}{(1/\tau_v - 1/\tau_s)^2 + \omega^2}\right] + \frac{U_{dc2} \tau_i}{\tau_v - \tau_i} - \frac{U_{dc3}}{\tau_v} \left[\frac{(1/\tau_v - \omega_{ci}) \cos \beta_2 + \omega_{ci} \sin \beta_2}{(1/\tau_v - \omega_{ci})^2 + \omega_{ci}^2}\right]$$

$$-\frac{U_{dc4}}{\tau_v} \left[\frac{(1/\tau_v - \omega_{ci}) \sin \beta_2 - \omega_{ci} \cos \beta_2}{(1/\tau_v - \omega_{ci})^2 + \omega_{ci}^2}\right] + \frac{U_{dc5}}{\omega_{ci} \tau_v - 1} + \frac{U_{dc6}}{-\lambda_1 \tau_v - 1} + \frac{U_{dc7}}{-\lambda_2 \tau_v - 1}$$

References

- Mai, T.; Wisser, R.; Sandor, D.; Brinkman, G.; Heath, G.; Denholm, P.; Hostick, D.J.; Darghouth, N.; Schlosser, A.; Strzepek, K. *Renewable Electricity Futures Study Volume 1: Exploration of High-Penetration Renewable Electricity Futures*; National Renewable Energy Laboratory: Golden, CO, USA, 2017.
- Li, H.; Eseye, A.T.; Zhang, J.; Zheng, D. Optimal energy management for industrial microgrids with high-penetration renewables. *Prot. Control Mod. Power Syst.* **2017**, *2*, 12. [[CrossRef](#)]
- Tazil, M.; Kumar, V.; Bansal, R.C.; Kong, S.; Dong, Z.Y.; Freitas, W.; Mathur, H.D. Three-phase doubly fed induction generators: An overview. *IET Electr. Power Appl.* **2010**, *4*, 75–89. [[CrossRef](#)]
- Strezoski, V.L.; Prica, D.M. Short-circuit analysis in large-scale distribution systems with high penetration of distributed generators. *IEEE/CAA J. Autom. Sin.* **2017**, *4*, 243–251. [[CrossRef](#)]
- Wang, X.; Pan, X.; Wan, J.; Qi, J.; Zhang, H.; Li, S. A wind farm short-circuit current calculation practical model applied to high voltage power grid simulation. In Proceedings of the 2014 International Conference on Mechatronics, Electronic, Industrial and Control Engineering, Shenyang, China, 17–19 November 2014. [[CrossRef](#)]
- Shen, S.; Lin, D.; Wang, H.; Hu, P.; Jiang, K.; Lin, D.; He, B. An adaptive protection scheme for distribution systems with DGs based on optimized Thevenin equivalent parameters estimation. *IEEE Trans. Power Deliv.* **2017**, *32*, 411–419. [[CrossRef](#)]
- Kauffmann, T.; Karaagac, U.; Kocar, I.; Jensen, S.; Mahseredjian, J.; Farantatos, E. An accurate type III wind turbine generator short circuit model for protection applications. *IEEE Trans. Power Deliv.* **2017**, *32*, 2370–2379. [[CrossRef](#)]
- Zhou, N.; Wu, J.; Wang, Q. Three-phase short-circuit current calculation of power systems with high penetration of VSC-based renewable energy. *Energies* **2018**, *11*, 537. [[CrossRef](#)]
- Dosoglu, M.K.; Guvenc, U.; Sonmez, Y.; Yilmaz, C. Enhancement of demagnetization control for low-voltage ride-through capability in DFIG-based wind farm. *Electr. Eng.* **2018**, *100*, 491–498. [[CrossRef](#)]
- General Administration of Quality Supervision, Inspection and Quarantine of the People's Republic of China and the Standardization Administration of the People's Republic of China. *Technical Rule for Connecting Wind Farm to Power System*; Xinhua Press: Beijing, China, 2012.
- VDE Verlag GmbH. *Technical Requirements for the Connection to and Parallel Operation with Low-Voltage Distribution Networks*; VDE Verlag GmbH: Berlin, Germany, 2017.
- Swain, S.; Ray, K.P. Short circuit fault analysis in a grid connected DFIG based wind energy system with active crowbar protection circuit for ride-through capability and power quality improvement. *Electr. Power Energy Syst.* **2017**, *84*, 64–75. [[CrossRef](#)]
- Zhu, Q.; Ding, M.; Han, P. Equivalent modeling of DFIG-based wind power plant considering crowbar protection. *Math. Probl. Eng.* **2016**, *2016*, 8426492. [[CrossRef](#)]
- Yuan, Y.H.; Wu, F. Short-circuit current analysis for DFIG wind farm considering the action of a crowbar. *Energies* **2018**, *11*, 425. [[CrossRef](#)]

15. Yin, J.; Bi, T.; Xue, A.; Yang, Q. Study on short circuit current and fault analysis method of double fed induction generator with low voltage ride-through control strategy. *Trans. China Electr. Tech. Soc.* **2015**, *30*, 118–125.
16. Ouyang, J.; Zheng, D.; Xiong, X.; Xiao, C.; Yu, R. Short-circuit current of doubly fed induction generator under partial and asymmetrical voltage drop. *Renew. Energy* **2016**, *88*, 1–11. [[CrossRef](#)]
17. Kong, X.; Zhang, Z.; Yin, X.; Wen, M. Study of fault current characteristics of the DFIG considering dynamic response of the RSC. *IEEE Trans. Energy Convers.* **2014**, *29*, 278–287.
18. Abad, G.; Lopez, J.; Rodríguez, A.M.; Marroyo, L.; Iwanski, G. *Doubly Fed Induction Machine: Modeling And Control For Wind Energy Generation*; Wiley-IEEE Press: Hoboken, NJ, USA, 2014; pp. 246–247.
19. Xiao, S.; Geng, H.; Zhou, H.; Yang, G. Analysis of the control limit for rotor-side converter of doubly fed induction generator-based wind energy conversion system under various voltage dips. *IET Renew. Power Gener.* **2013**, *7*, 71–81. [[CrossRef](#)]
20. Hu, J.; He, Y. DFIG wind generation systems operating with limited converter rating considered under unbalanced network conditions—Analysis and control design. *Renew. Energy* **2011**, *36*, 829–847. [[CrossRef](#)]
21. Chen, P.; Zhang, Z.; Yin, X.; Xiao, F.; Yang, Z.; Wang, L. Steady fault current calculation model of doubly-fed induction generator considering grid-side converter current and different control strategies. *Autom. Electr. Power Syst.* **2016**, *40*, 8–16.
22. Honrubia-Escribano, A.; Jiménez-Buendía, F.; Gómez-Lázaro, E.; Fortmann, J. Field validation of a standard type 3 wind turbine model for power system stability, according to the requirements imposed by IEC 61400-27-1. *IEEE Trans. Energy Convers.* **2018**, *33*, 137–145. [[CrossRef](#)]
23. Zhang, C.W.; Zhang, X. *PWM Rectifier and Control*; Machine Press: Beijing, China, 2003; pp. 114–117.
24. Xiao, F.; Zhang, Z.; Yin, X. Fault current characteristics of the DFIG under asymmetrical fault conditions. *Energies* **2015**, *8*, 10971–10992. [[CrossRef](#)]
25. Liu, S.M.; Bi, T.S.; Jia, K.; Yang, Q.X. Coordinated fault-ride-through strategy for doubly-fed induction generators with enhanced reactive and active power support. *IET Renew. Power Gener.* **2016**, *10*, 203–211. [[CrossRef](#)]
26. Lopez, J.; Sanchis, P.; Roboam, X.; Marroyo, L. Dynamic behavior of the doubly fed induction generator during three-phase voltage dips. *IEEE Trans. Energy Convers.* **2007**, *22*, 709–717. [[CrossRef](#)]
27. National Energy Administration. *Test Procedures of WIND Turbine Low Voltage Ride Through Ability*; Xinhua Press: Beijing, China, 2015.



© 2018 by the authors. Licensee MDPI, Basel, Switzerland. This article is an open access article distributed under the terms and conditions of the Creative Commons Attribution (CC BY) license (<http://creativecommons.org/licenses/by/4.0/>).